Structure of Polymer-Grafted Nanoparticle Melts

Jiarul Midya,* Michael Rubinstein, Sanat K. Kumar, and Arash Nikoubashman*

ACCESS | Metrics & More | Article Recommendations | Supporting Information

ABSTRACT: The structure of neat melts of polymer-grafted nanoparticles (GNPs) is studied *via* coarse-grained molecular dynamics simulations. We systematically vary the degree of polymerization and grafting density at fixed nanoparticle (NP) radius and study in detail the shape and size of the GNP coronas. For sufficiently high grafting density, chain sections close to the NP core are extended and form a dry layer. Further away from the NP, there is an interpenetration layer, where the polymer coronas of neighboring GNPs overlap and the chain sections have almost unperturbed conformations. To better understand this partitioning, we develop a two-layer model, representing the grafted polymer around an NP by spherical dry and interpenetration layers. This model quantitatively predicts that the thicknesses of the two layers depend on one universal parameter, x, the degree of overcrowding of grafted chains relative to chains in the melt. Both simulations and theory show that the chain extension free energy is nonmonotonic with increasing chain length at a fixed grafting density, with a well-defined maximum. This maximum is indicative of the crossover from the dry layer-dominated to interpenetration layer-dominated regime, and it could have profound consequences on our understanding of a variety of anomalous transport properties of these GNPs. Our theoretical approach therefore provides a facile means for understanding and designing solvent-free GNP-based materials.

Simulation   Two-layer model

KEYWORDS: *polymer-grafted nanoparticles, polymer brushes, interpenetration, molecular dynamics simulations, scaling theory, two-layer model*
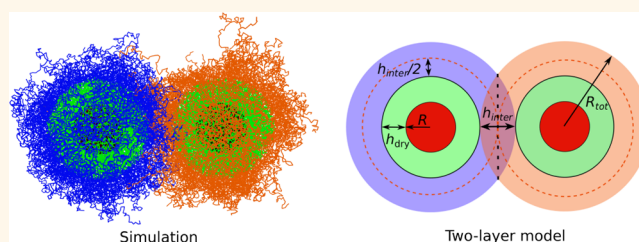
Over the past few decades, polymer nanocomposites have gained significant attention due to their wide range of applications in drug delivery,[1−3] desalination,[4−6] and photonic[7,8] and phononic materials.[9,10] These applications often require a homogeneous dispersion of nanoparticles (NPs) in the polymer matrix to optimize their physical properties. In practice, however, such uniform mixing is difficult to achieve, due to the chemical incompatibility between the two components. Instead, one often encounters an undesired aggregation of the (inorganic) NPs in the (organic) polymer matrix, which can lead to a deterioration of material properties and mechanical stability of the composite. Such phase separation can be prevented by grafting the polymers to the surface of the NPs, that is, turning these two component systems into effectively one component systems.[11−19] These hybrid particles, known as polymer-grafted NPs (GNPs) or hairy NPs, typically exhibit a core−shell morphology with a hard core and a soft corona. While many previous theoretical descriptions focused on GNPs mixed with small molecule solvents,[20,21] we are interested in melts of GNPs where the surrounding medium is composed of other GNPs. This situation has received significantly less theoretical attention to date.[22−25]

The hybrid nature of GNPs can substantially improve, for example, the mechanical,[26−33] optical,[34,35] thermal,[36,37] electrical,[36,37] and rheological[38,39] properties of a material in comparison to the corresponding bulk polymer or traditional physically mixed NP/polymer composites. These properties are controlled by the grafting density of the chains and their degree of polymerization, the size and shape of the cores, the interactions between the polymers and the cores, *etc.* For example, the elastic moduli of GNP systems can be tuned by varying the NP loading through the grafting density and/or the length of the grafted polymers. Even at a fixed NP loading, the mechanical properties of GNPs depend on their microscopic details, as was demonstrated in recent experiments and simulations.[30] In that work, significant deviations of the elastic moduli were observed compared to predictions based on a simple mean-field description,[40] with sparsely grafted GNP
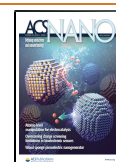
systems exhibiting higher elastic moduli compared to densely grafted GNPs.[30] This enhancement was attributed to the coil-like conformations of the sparsely grafted chains, which promoted a higher degree of polymer interpenetration compared to densely grafted NPs with short chains. It is thus clear that the microscopic details of GNPs play an important role in their macroscopic material properties.

In previous experiments and simulations, the phase behavior of GNPs in neat melts or within polymer matrices was studied.[41−47] It was found, for example, that GNPs in such solvent-free conditions exhibit structural transitions from a simple liquid to a glass forming liquid or from star-polymer-like to colloid-like behavior with variations of grafted polymer length and grafting density.[42,44,47] Recent field-based simulations have shown that GNPs in a homopolymer matrix exhibit an entropically driven mixing−demixing transition,[46] which was controlled by the core size and the ratio of the lengths of the free and grafted polymers. In the demixed state, the GNPs self-assembled into a variety of nanostructures, such as sheets, wires, and capsules, depending on, for example, the size and shape of the NPs, grafting density, length of the grafted polymers, and intermolecular interactions.[48−50] However, there is only a small number of studies on pure GNP melts that focus on the size, shape, and interpenetration of the polymer coronas of the GNPs on a microscopic level. Understanding these aspects could elucidate a variety of anomalous transport properties of these GNP systems.[51]

To fill this void, we investigate the structure of neat melts of GNPs *via* coarse-grained molecular dynamics (MD) simulations. We systematically vary the degree of polymerization and grafting density at fixed NP core radius and study in detail the shape, size, and interpenetration of the polymer coronas surrounding the NP cores. Further, we analyze the conformations of the grafted polymers and compare them with their pure bulk polymer analogs to assess both the effects of chain grafting and the presence of other GNPs. To rationalize our simulation results, we introduce a two-layer model, in which the polymer corona is divided into a dry layer, that is, the region where almost no monomers from surrounding GNPs were present, and an interpenetration layer, which is characterized by a significant overlap between grafted chains of surrounding GNPs. Sections of grafted chains belonging to the dry layer are extended, whereas parts in the interpenetration layer are almost unperturbed. This model predicts that the thicknesses of the two layers depend on a single parameter, which essentially describes the degree of overcrowding of grafted chains compared to unperturbed chains in a melt. The analytical predictions for the thicknesses of the dry and interpenetration layers are in excellent quantitative agreement with our simulation results across a broad parameter range with the use of a single adjustable constant.

RESULTS

Two-Layer Model. In our theoretical model, the grafted layer of a GNP consists of a dry and an interpenetration layer with thicknesses h_{dry} and h_{inter}, respectively (see the schematic shown in Figure 1a). To estimate the overall brush thickness of the GNPs, $h = h_{dry} + h_{inter}/2$, we consider a single isolated GNP with a spherical polymer brush. In this case, the volume of the spherical shell between R and $R + h$ is completely occupied by all monomers from the grafted chains, and the brush thickness is simply given by the space-filling condition:
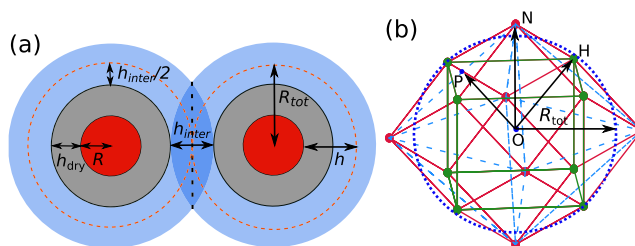

Figure 1. (a) Schematic representation of the two-layer model, indicating the NP radius, R, the total radius of the GNP, R_{tot}, and the thicknesses of the dry and interpenetration layers, h_{dry} and h_{inter}, respectively. (b) Voronoi cell (rhombic dodecahedron) for the fcc packing of spheres. The center of the cell is indicated by O, and the midpoint of one of the rhombic faces is indicated by P. The vector from O to P points to the nearest neighbor, and its length is given by the lattice constant of the fcc crystal, $|OP| = a_0$. The vector from O to H points to the next-nearest neighbor and has a length of $|OH| = \sqrt{3/2}\,a_0$, while the vector pointing from O to N has a length of $|ON| = \sqrt{2}\,a_0$. The sphere (blue dashed line) with radius R_{tot} has the same volume as the Voronoi cell.

$$\frac{4}{3}\pi[(R + h)^3 - R^3] = Z\frac{N}{\rho} \tag{1}$$

where R is the radius of the NP, $Z = 4\pi R^2 \rho_g$ is the number of chains grafted to the NP with grafting density ρ_g, N is the number of Kuhn monomers per grafted chain, and ρ is the Kuhn monomer number density (assumed uniform) within the spherical shell. Thus, the total radius of the GNP is:

$$R_{tot} = \left(R^3 + \frac{3ZN}{4\pi\rho}\right)^{1/3} \tag{2}$$

and the brush thickness is given by:

$$h = R_{tot} - R = \left(R^3 + \frac{3ZN}{4\pi\rho}\right)^{1/3} - R \tag{3}$$

This estimate for h ignores that the actual shape of the polymer layers at dense packing must correspond to the Voronoi cells defined by the position of the NPs, for example, a rhombic dodecahedron for the face-centered cubic (fcc) packing of spheres (see Figure 1b). In the simulations, the brush thickness h can be defined in various ways (see Simulations section and Supporting Information for details). The resulting values for h are all within 5−10% of each other, and they all vary similarly with the parameters of the system, namely N and Z (see Table 1). In our simulations, we chose the radially averaged center of the interpenetration layer to determine the brush thickness, and we can match the theoretical predictions by introducing an empirical shape factor, $\alpha \approx 0.93$, that reduces all theoretical curves for h, h_{dry} and h_{inter} (see eqs 3, 8, and 10) by 7%.

Next, we discuss the interpenetration between the polymer coronas from neighboring GNPs using the two-layer model. This model assumes that the dry and interpenetration layers are spherical and that the overlap between neighboring GNPs is primarily pairwise. If we further posit that, on average, each grafted chain has $n_{dry} = N - n_{inter}$ Kuhn monomers in the dry layer and the remaining n_{inter} monomers in the interpenetration layer, then the space-filling condition for the dry layer can be rewritten by analogy with eq 1:
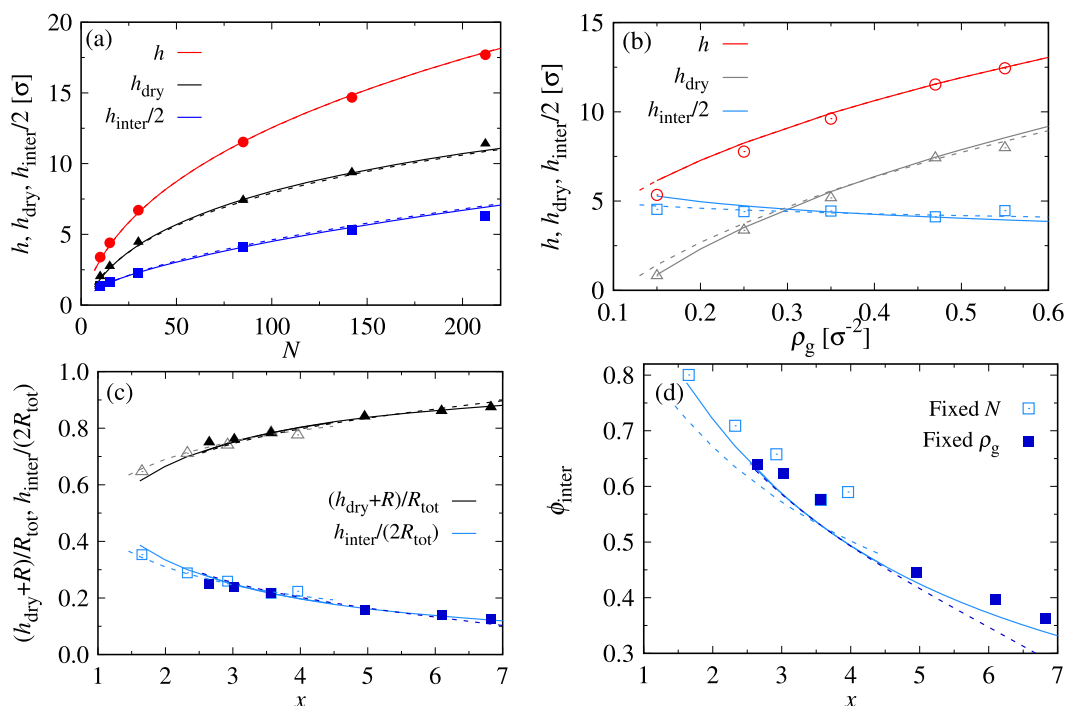
Figure 2. (a, b) Total brush thicknesses $h = h_{dry} + h_{inter}/2$, thickness of the dry layer h_{dry}, and half thickness of the interpenetration layer $h_{inter}/2$ plotted (a) as functions of chain length N at fixed grafting density $\rho_g = 0.47\ \sigma^{-2}$ and (b) as functions of ρ_g at fixed $N = 85$. In both cases, $R = 7.5\sigma$ fixed. (c) Reduced thicknesses $h_{inter}/(2R_{tot})$ and $(h_{dry} + R)/R_{tot}$ as functions of x. $[(h_{dry} + R)/R_{tot} + h_{inter}/(2R_{tot}) = 1.]$ Filled and open symbols correspond to the data shown in panels (a) and (b), respectively. (d) Volume fraction of the interpenetration layer, ϕ_{inter}, as a function of x for systems shown in (a, b). In all panels, symbols show our simulation results (initialized from random NP locations), while solid lines are theoretical predictions of our two-layer model. The dashed lines are the theoretical predictions of the modified model of Kapnistos et al.[25]

Table 1. Brush Thickness of the GNPs[a]

N	ρ_g (σ^{-2})	h_v (σ)	random			fcc		
			h_{nn} (σ)	h_ρ (σ)	δ (σ)	h_{nn} (σ)	h_ρ (σ)	δ (σ)
10	0.47	3.6	2.3	3.4	2.7	2.5	3.4	2.6
15	0.47	4.6	3.2	4.4	3.3	3.3	4.4	3.0
30	0.47	7.0	5.1	6.7	4.5	5.7	6.8	4.2
85	0.47	12.4	9.1	11.5	8.2	10.4	11.6	7.1
142	0.47	15.9	12.0	14.7	10.6	13.7	15.0	8.8
212	0.47	19.3	14.5	17.7	12.3	16.6	18.1	10.0
85	0.15	6.6	4.0	5.3	9.1	–	–	–
85	0.25	8.8	6.1	7.8	8.8	–	–	–
85	0.35	10.7	7.8	9.6	8.8	–	–	–
85	0.55	13.4	9.9	12.4	8.7	–	–	–

[a]Extracted from the average volume of Voronoi cells constructed around the NPs, $h_v = [3\langle V_v\rangle/(4\pi)]^{1/3} - R$, from the distance between nearest neighbors, $h_{nn} = r_{nn}/2 - R$, and from the peak position h_ρ of the product of the radial density profiles $\rho_g\rho_o$. The full width at half maximum δ of the product $\rho_g\rho_o$ is also shown. Results are included for random and fcc lattice starting configurations, as indicated.

$$\frac{4}{3}\pi[(R + h_{dry})^3 - R^3] = Z\frac{n_{dry}}{\rho} \qquad (4)$$

An analogous expression can be formulated for the interpenetration layer, which is equally shared between neighboring GNPs, by replacing in eq 1 h with $h_{inter}/2$ and R with $R + h_{dry}$:

$$\frac{4}{3}\pi[(R + h_{dry} + h_{inter}/2)^3 - (R + h_{dry})^3] = Z\frac{n_{inter}}{\rho} \qquad (5)$$

Here, we have assumed that all grafted chains enter the interpenetration layer, which is corroborated by our simulations, where 98−100% of the grafted chains had at least one bead in the interpenetration layer. We can solve eqs 4 and 5 under the assumption that the chain sections in the interpenetration layer are unperturbed with root-mean-square end-to-end distance:

$$h_{inter} = bn_{inter}^{1/2} \qquad (6)$$

where b is the Kuhn length of the polymer. It is important to note that we can combine eqs 4 and 5, and then the result for $h_{dry} + h_{inter}/2$ is identical to the result for h (see eq 3).

A detailed derivation of the analytical solution of the two-layer model is provided in the Supporting Information, and below we will focus on its key results. The main parameter of our analytical solution is:

$$x = \frac{Z}{\pi\rho b^2 R_{tot}} = \frac{Z}{\pi\rho b^2[R^3 + 3ZN/(4\pi\rho)]^{1/3}} \qquad (7)$$

which monotonically decreases with increasing N at fixed Z, and monotonically increases with increasing Z at fixed N. To understand the physical basis of this parameter, we consider a volume R_{tot}^3 in an unperturbed polymer melt. This volume is occupied by $\rho R_{tot}^3/N_{tot}$ chains, where N_{tot} is defined through the equation $R_{tot}^2 = N_{tot}b^2$. The number of chains that fill this volume in an unperturbed melt is thus on the order of $\rho b^2 R_{tot}$, and therefore x is proportional to the ratio of the actual number of graft chains Z to the number of chains that occupy the same volume in an unperturbed melt. Hence, $x \approx O(1)$ corresponds to an (almost) unperturbed melt, whereas $x \gg 1$

Table 2. Information about the Simulated Systems[a]

ρ_g (σ^{-2})	N	x	random		fcc		ρ (σ^{-3})	ϕ_{NP}
			N_{NP}	$\mathcal{N}$	N_{NP}	$\mathcal{N}$		
0.47	10	6.88	50	166,000	32	106,240	0.848	0.312
0.47	15	6.10	50	249,000	32	159,360	0.873	0.237
0.47	30	4.96	50	498,000	32	318,720	0.895	0.138
0.47	85	3.57	25	705,500	32	903,040	0.910	0.054
0.47	142	3.02	25	1,1786,00	32	1,508,608	0.914	0.033
0.47	212	2.65	25	1,759,600	32	2,252,288	0.916	0.023
0.15	85	1.65	50	450,500	–	–	0.877	0.147
0.25	85	2.33	40	598,400	–	–	0.897	0.096
0.35	85	2.93	32	671,480	–	–	0.906	0.071
0.55	85	3.97	20	659,600	–	–	0.913	0.047

[a]Grafting density ρ_g, number of monomers per grafted chain N, overcrowding parameter x, number of NPs N_{NP}, total number of monomers in the system $\mathcal{N}$, average monomer density ρ, and packing fraction of NPs in the system ϕ_{NP}. Random and fcc lattice starting configurations led to the same values for ρ and ϕ_{NP} within our measurement accuracy.

implies that the volume is overcrowded and the grafted chains are strongly extended.

We can write the analytical solution for h_{inter} using the parameter x as:

$$h_{inter} = 3R_{tot}(1 + x)\left[1 - \sqrt{1 - \frac{4}{3}\left(\frac{1}{1+x}\right)^2}\right] \tag{8}$$

The volume fraction of the interpenetration layer in the GNP system, $\phi_{inter} = (Zn_{inter}/\rho)/(4\pi R_{tot}^3/3)$, is then given by:

$$\phi_{inter} = \frac{27}{4}x(1 + x)^2\left[1 - \sqrt{1 - \frac{4}{3}\left(\frac{1}{1+x}\right)^2}\right]^2 \tag{9}$$

Hence, both h_{inter}/R_{tot} and ϕ_{inter} depend *only* on the overcrowding parameter x. The rest of the GNP volume (fraction) is occupied by the NP core and a dry layer of extended chains. For $R < R_{tot} - h_{inter}/2$, the thickness of the dry layer is given by:

$$h_{dry} = R_{tot} - R - h_{inter}/2 \tag{10}$$

whereas no dry layer exists if $R > R_{tot} - h_{inter}/2$. In the latter case, our two-layer model breaks down because the polymer corona is too thin to accommodate even unperturbed melt-like chains. Further, our theoretical model is physically meaningful only if there is enough polymer to uniformly fill the interstitial spaces between the NP cores. We can estimate this lower bound by considering the volume occupied by the grafted chains, $V_{poly} = ZN/\rho$, and the void space between closely packed bare NPs, $V_{void} = 8(\sqrt{8} - 2\pi/3)R^3$. (In an fcc configuration, a cubic unit cell with edge length $2\sqrt{2}R$ is occupied by four spheres with radius R, and hence $V_{void} = (2\sqrt{2}R)^3 - 16\pi R^3/3 = 8(\sqrt{8} - 2\pi/3)R^3$.) Therefore, we consider only cases where the conditions $R < R_{tot} - h_{inter}/2$ and $V_{poly}/V_{void} \geq 1$ are both satisfied.

Figure 2a−d shows a comparison of the theoretical predictions of h, h_{dry}, $h_{inter}/2$, and ϕ_{inter} with the corresponding simulation results (see Simulations section for details). We fixed the NP radius to $R = 7.5\sigma$ (σ being the diameter of a monomeric unit) and varied either the chain length N at fixed grafting density $\rho_g = 0.47\ \sigma^{-2}$ or varied ρ_g at fixed $N = 85$. For the theoretical calculations, we used the average monomer number density of our simulations $\rho = 0.9\ \sigma^{-3}$ (see Table 2)

and the Kuhn length $b = 1.28\sigma$ of this polymer model.[52] Using instead the actual monomer number density measured in the simulations (see Table 2) leads to a change in brush thicknesses smaller than 2% and was therefore disregarded for simplicity. For these parameters, our two-layer model is applicable for $N \gtrsim 7$ for GNPs with fixed $\rho_g = 0.47\ \sigma^{-2}$ and for $\rho_g \gtrsim 0.12\ \sigma^{-2}$ for GNPs with fixed $N = 85$. In all investigated cases, the theoretical predictions and simulation results for h, h_{dry}, and $h_{inter}/2$ are in excellent agreement after we multiplied the theoretical curves by the shape factor $\alpha \approx 0.93$ (see Figure 2). For GNPs with fixed grafting density $\rho_g = 0.47\ \sigma^{-2}$, both h_{dry} and $h_{inter}/2$ increase with increasing N, with $h_{dry} > h_{inter}/2$ for the investigated range of N (see Figure 2a). For GNPs with fixed chain length $N = 85$, h_{dry} increases with increasing ρ_g, while $h_{inter}/2$ decreases (see Figure 2b). The reduced thickness of the interpenetration layer, $h_{inter}/(2R_{tot})$, is a universal function monotonically decreasing with increasing x, with $h_{inter}/(2R_{tot}) \propto x^{-1}$ for large x (see Supporting Information). Similarly, the normalized sum of dry layer thickness and NP radius, $(h_{dry} + R)/R_{tot}$, is a universal function monotonically increasing with increasing x (see Figure 2c), with $(h_{dry} + R)/R_{tot} \propto 1 - x^{-1}$ for large x (see Supporting Information). The volume fraction of the interpenetration layer, ϕ_{inter}, is a universal function of x which monotonically decreases with increasing x (see Figure 2d), with $\phi_{inter} \propto 3x^{-1}$ for large x (see Supporting Information). The excellent agreement of the theoretical curves with the simulation data confirms that the structures of GNPs of different grafting densities ρ_g and chain lengths N are identical if they have the same x.

Due to grafting and space-filling constraints, the densely grafted chains are extended in comparison to unperturbed polymers in a melt. To quantify this effect, we now consider the chain extension free energy:

$$E_{ext} = \frac{3k_BTh^2}{2Nb^2} = \frac{3k_BT}{2Nb^2}\left[\left(R^3 + \frac{3ZN}{4\pi\rho}\right)^{1/3} - R\right]^2 \tag{11}$$

This chain extension energy is a function of the ratio $y = 3ZN/(4\pi\rho R^3)$ of the polymer shell volume ZN/ρ to the NP core volume $4\pi R^3/3$:

$$E_{ext} = \frac{3k_BT}{8\pi}\frac{3Z}{\rho Rb^2}y^{-1}[(1 + y)^{1/3} - 1]^2 \tag{12}$$

where the coefficient $3Z/(Rb^2\rho)$ is the ratio of the polymer shell volume ZN/ρ to the volume of a cone with base area b^2N and height R. If the polymer shell volume is much smaller than the NP core volume, $y \ll 1$, then E_{ext} can be expanded with respect to y, leading to the planar brush result:

$$E_{ext}^{pln} \approx \frac{k_BT}{8\pi} \frac{Zy}{\rho Rb^2} = \frac{3k_BT}{2} \left(\frac{Z}{4\pi\rho R^2 b} \right)^2 N \qquad (13)$$

In the opposite limit, $y \gg 1$, the chain extension energy decreases with increasing N because the layer thickness scales as $h \propto N^{1/3}$:

$$E_{ext}^{sph} \approx \frac{9k_BT}{8\pi} \frac{Zy^{-1/3}}{\rho Rb^2} = \frac{3k_BT}{2} \left(\frac{3Z}{4\pi\rho b^3} \right)^{2/3} N^{-1/3} \qquad (14)$$

Thus, for small polymer to NP volume ratio $y \ll 1$, the chain extension free energy increases as $E_{ext} \propto y \propto N$, while for large volume ratio $y \gg 1$, it decreases as $E_{ext} \propto y^{-1/3} \propto N^{-1/3}$. Therefore, E_{ext} goes through a maximum at $y_{max} = 6\sqrt{3} + 9 \approx 19.4$, corresponding to:

$$N_{max} = 4\pi(2\sqrt{3} + 3)\frac{\rho R^3}{Z} \approx 81\frac{\rho R^3}{Z} \qquad (15)$$

This chain length corresponds to a polymer layer thickness:

$$h_{max} = [(6\sqrt{3} + 10)^{1/3} - 1]R = \sqrt{3}\,R \qquad (16)$$

which is only $\sqrt{3}$ times larger than the NP radius. The value of the chain extension free energy at this maximum is:

$$E_{ext}^{max} = \frac{3(2\sqrt{3} - 3)k_BT}{8\pi} \frac{Z}{\rho Rb^2} \approx 0.7k_BT\frac{\rho_g}{\rho b^2}R \qquad (17)$$

For the case of interest for our simulations, that is, $\rho_g = 0.47$ σ^{-2}, $R = 7.5\sigma$, and $\rho = 0.9\,\sigma^{-3}$, the theoretically predicted maximum of E_{ext} is located at $N_{max} \approx 93$, as shown in Figure 3a. The simulation result for E_{ext} has a maximum at $N_{max} = 85$, which is in good agreement with the theoretical results when we multiply the latter by the square of the shape factor $\alpha^2 \approx 0.86$. The maximum of E_{ext} occurs at the same value of the volume ratio $y_{max} \approx 19.4$, independent of whether the chains are strongly extended ($E_{ext}^{max} \gg k_BT$) or not extended at all ($E_{ext}^{max} < k_BT$), and is a result of the geometric crossover from a planar polymer layer around an NP (for small y) to a thick spherical polymer shell (for large y).

The case of interest for this work corresponds to GNPs that have a dry layer. It is interesting to note that for such densely grafted NPs, the spherical-like increase of the overall layer thickness $h \propto N^{1/3}$ can occur while chains are still strongly extended before GNPs enter the star polymer regime. This means that the geometric crossover of E_{ext} between the planar increase $E_{ext}^{pln} \propto N$ and spherical decrease $E_{ext}^{sph} \propto N^{-1/3}$ is predicted by the two-layer model with extended polymers over the wide range of parameter N on both sides of the free energy maximum. Figure 3a demonstrates that the maximum of E_{ext} as a function of N and the decreasing chain extension free energy beyond this maximum are features that describe the GNPs of interest. In contrast, if the grafting density ρ_g (or Z) is varied at constant chain length N, then E_{ext} does not show a maximum but increases monotonically with increasing ρ_g (or Z) instead (see Figure 3b).

Finally, we want to briefly discuss an alternative model for the theoretical description of GNPs. Kapnistos et al. proposed
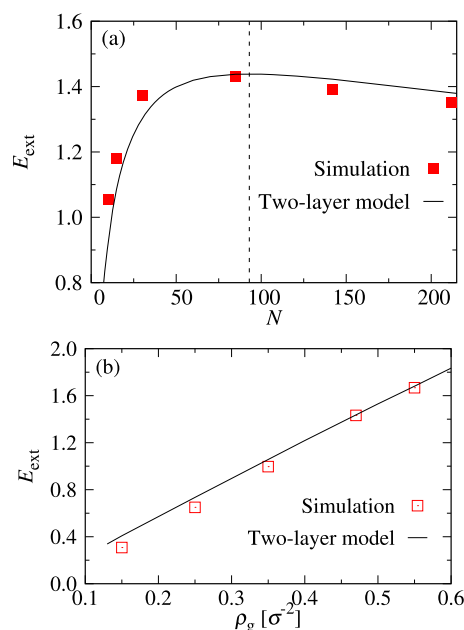

Figure 3. Chain extension free energy, E_{ext}, as a function of (a) N for fixed $\rho_g = 0.47$ σ^{-2} and (b) ρ_g for fixed $N = 85$. Symbols are simulation results (initialized from random NP locations), and the black solid lines indicate the theoretical predictions from the two-layer model and the modified model of Kapnistos et al.[25] The vertical dashed line in (a) indicates the position of the maximum of the theoretical curve.

a scaling model to study the structure of multiarm star polymers in a melt,[25] which can be adapted to our systems by including the contribution of the NP core. With this modification, the expression for the total brush thickness h becomes identical with our two-layer model given by eq 3, due to the incompressibility constraint and the conservation of the total volume. The two approaches differ, however, in the construction of the interpenetration layer. We assumed in our two-layer model that all grafted chains enter the interpenetration layer, whereas in the theory by Kapnistos et al., the number of chains in the interpenetration layer increases with decreasing overcrowding parameter x as $\tilde{Z} \propto Zx^{-1/3}$. Kapnistos et al. obtained the scaling of the interpenetration layer from the parabolic potential approximating the polymer layer by a planar brush, which leads to the scaling result $h_{inter} \propto bN^{1/2}x^{-1/6}$. We fitted this expression for h_{inter} to our simulation data (see Figure 2), giving a prefactor of $\beta \approx 0.85$.

Despite these differences, we observe that the predictions from both models for h, h_{dry}, and $h_{inter}/2$ are in good agreement with our simulation results for the investigated range of the overcrowding parameter $1.5 \lesssim x \lesssim 7$, see Figure 2a,b. The two models start to deviate for large x (see comparison between the two approaches in the Supporting Information), for which the polymer corona becomes more planar ($h \ll R$). That regime is, however, outside of interest of this study. We emphasize that our simple analytical model for the GNPs provides an excellent description of h, h_{dry}, h_{inter}, and ϕ_{inter} across the range of interest to most experimental situations (see Figures 2 and 3).

Simulations. We consider GNP melts for different values of the chain length N and grafting density ρ_g at fixed NP radius $R = 7.5\sigma$. The details of the simulations are provided in the Methods section. Figure 4 shows snapshots of single GNPs from these melts for various grafted chain lengths (a) $N = 15$,
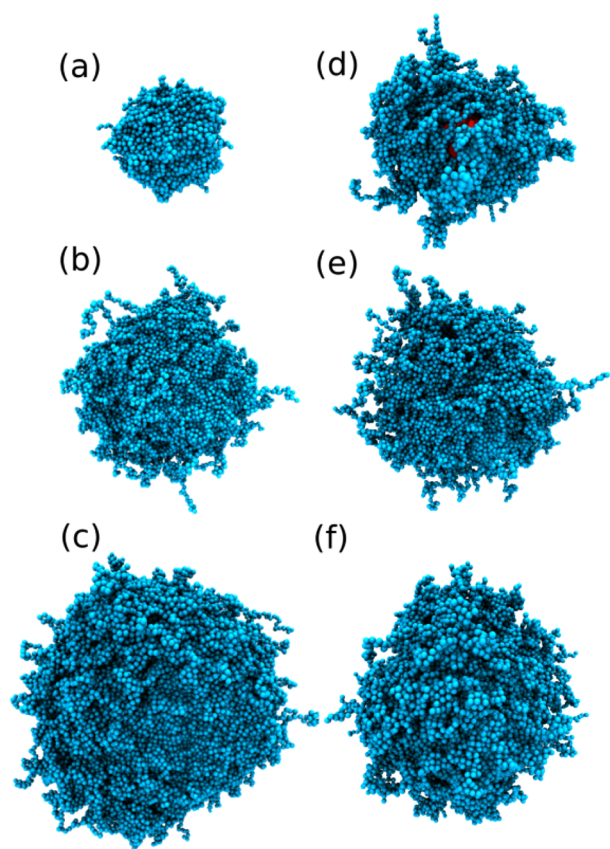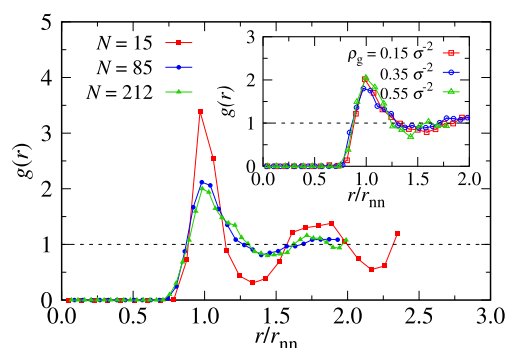
Figure 5. Radial distribution function, $g(r)$, between centers of NPs with random starting configurations. The inset shows $g(r)$ for GNP systems with different grafting densities at a fixed chain length $N = 85$. In both plots, the x-axis is scaled with the average nearest-neighbor distance, r_{nn}.

Figure 4. Simulation snapshots of a single GNP in a bulk system with varying chain lengths, (a) $N = 15$, (b) $N = 85$, and (c) $N = 212$ at $\rho_g = 0.47\ \sigma^{-2}$, and with varying grafting densities, (d) $\rho_g = 0.15\ \sigma^{-2}$, (e) $\rho_g = 0.35\ \sigma^{-2}$, and (f) $\rho_g = 0.55\ \sigma^{-2}$ at $N = 85$. Snapshots have been taken from the systems initialized from random starting configurations, and they have been rendered using Visual Molecular Dynamics v 1.9.3.[53]

(b) $N = 85$, and (c) $N = 212$ at grafting density $\rho_g = 0.47\ \sigma^{-2}$ and for various grafting densities (d) $\rho_g = 0.15\ \sigma^{-2}$, (e) $\rho_g = 0.35\ \sigma^{-2}$, and (f) $\rho_g = 0.55\ \sigma^{-2}$ at chain length $N = 85$ for systems with random starting configurations. In this context, we emphasize that, as discussed in the Methods section, the initial NP locations are at random, which should be contrasted with an ordered arrangement of initial NP locations on an fcc lattice, which is also considered in this work (see below). For fixed grafting density $\rho_g = 0.47\ \sigma^{-2}$, the overall size of the GNPs increases with increasing N, as expected. Similarly, for fixed chain length $N = 85$, the size of the GNPs increases with increasing ρ_g. Based on these snapshots, it appears that the spherical shape of the GNPs becomes increasingly distorted with the increase of N at fixed ρ_g, whereas the shape of the GNPs remains almost unaltered for fixed $N = 85$ and varying ρ_g (see Figure 6 and accompanying discussion for a quantitative analysis of the shape of the GNPs).

The radial distribution functions of the NP centers, $g(r)$, are presented in Figure 5 for three different grafted chain lengths $N = 15$, $N = 85$, and $N = 212$ at $\rho_g = 0.47\ \sigma^{-2}$, initialized from random NP locations. For all cases, we can see that $g(r)$ oscillates around one (black horizontal dashed line), indicating that the NPs have some local structure but are uniformly dispersed in the matrix of grafted polymers. The first peak of $g(r)$ at position r_{nn} represents the average separation between the nearest-neighbor NPs, and r_{nn} shifts to larger distances as N

is increased (see Table 1). Further, the first peak of $g(r)$ is relatively narrow for $N = 15$, but it becomes significantly broader for $N = 85$ and $N = 212$ at fixed ρ_g. Since the (normalized) peak width is characteristic of the rattling of the GNPs in a "cage", evidently the degree of GNP localization decreases with increasing chain length. This behavior can be rationalized by the increase of the volume fraction occupied by the interpenetration layer with increasing N, which leads to a softening of the effective interactions between the GNPs. A similar behavior is observed in the case of GNPs on the fcc lattice as well, but there the peaks are overall more pronounced due to the crystalline long-range order of the GNPs (not shown here). The inset of Figure 5 shows $g(r)$ for three different grafting densities, $\rho_g = 0.15\ \sigma^{-2}$, $\rho_g = 0.35\ \sigma^{-2}$ and $\rho_g = 0.55\ \sigma^{-2}$ at $N = 85$, for systems with random starting configurations. The nearest-neighbor distance r_{nn} increases with increasing ρ_g (see Table 1), but the (normalized) peak width is similar for all investigated ρ_g.

To quantify the size distribution of the GNPs, we have performed a Voronoi tessellation[54] around the centers of the NPs and then computed the (normalized) distributions of the volume of the Voronoi cells, V_v. Figure 6a shows the distributions for selected N at fixed $\rho_g = 0.47\ \sigma^{-2}$ for both the random and ordered starting configurations. The width of the distributions increases with N, indicating that the correlation between NPs is becoming weaker with increasing N. This behavior is consistent with the prediction from our two-layer model that the volume fraction of the interpenetration layer, ϕ_{inter}, monotonically increases with increasing N at fixed ρ_g (see Figure 2d). The volume distributions in the systems initialized from the fcc lattice are much more narrow and show a weaker N-dependence compared to the random GNP configurations, reflecting the high symmetry of the fcc lattice. Irrespective of the starting configurations, the mean value of the distribution, $\langle V_v \rangle$, increases almost linearly with N. Similar behavior is observed for the GNP systems with varying ρ_g (or varying $Z = 4\pi R^2 \rho_g$) at fixed $N = 85$. This linear relationship $\langle V_v \rangle = (4/3)\pi R^3 + ZN/\rho = (4/3)\pi R_{tot}^3$ is expected, because the number of monomers per GNP (and thus the volume occupied by them) increases linearly with N at fixed ρ_g (see inset in Figure 6a) or with ρ_g at fixed N.

The shape of the Voronoi cells and of the corona of the GNPs is probed *via* the asphericity parameter, S^2, defined as:
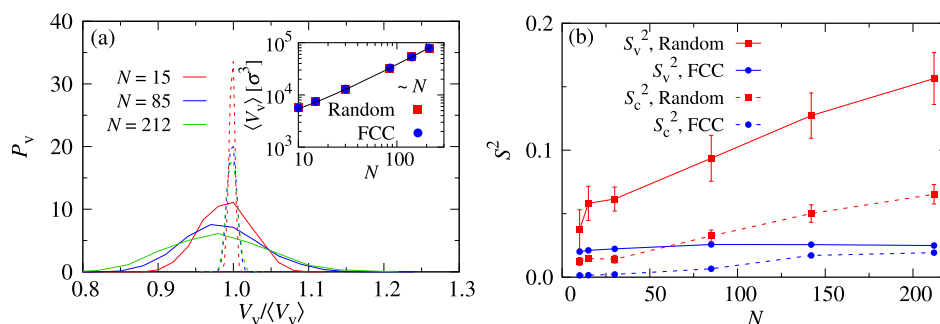
Figure 6. (a) Normalized distributions of the volume of Voronoi cells, V_v, of selected GNP systems with $\rho_g = 0.47\ \sigma^{-2}$, as indicated. The x-axis is scaled with the mean volume of the Voronoi cells, $\langle V_v \rangle$. Solid colored curves show the results for simulations with random initial positions, whereas dashed curves represent the same quantity for GNP systems initialized on an fcc lattice (area under the curve normalized to 0.3 instead of unity for better visualization). The inset presents the average volume of Voronoi cells, $\langle V_v \rangle$, as a function of N. The solid black line shows $\langle V_v \rangle = (4/3)\pi R_{tot}^3$. (b) Asphericity parameter, S^2, of the Voronoi cells (S_v^2 solid curves) and of the polymer coronas of the GNPs (S_c^2 dashed curves) as functions of N at fixed $\rho_g = 0.47\ \sigma^{-2}$. Results from random and fcc lattice starting configurations are shown as red and blue curves, respectively.

$$S^2 = \frac{3}{2}\frac{\lambda_1^4 + \lambda_2^4 + \lambda_3^4}{(\lambda_1^2 + \lambda_2^2 + \lambda_3^2)^2} - \frac{1}{2} \tag{18}$$

where λ_1, λ_2, and λ_3 are the eigenvalues of the gyration tensor (along the three principle axes) of the vertices of the Voronoi cell relative to the NP center or of all of the monomers forming the corona of a GNP with respect to their center of mass. The value of S^2 is bounded between zero and one. The lower limit $S^2 = 0$ is consistent with spherical symmetry ($\lambda_1 = \lambda_2 = \lambda_3$), while the upper limit $S^2 = 1$ indicates a rod-like shape. In Figure 6b, we present the average values of the asphericity parameter for the Voronoi cell (S_v^2) and the polymer corona (S_c^2) as functions of N at fixed $\rho_g = 0.47\ \sigma^{-2}$. Both S_v^2 and S_c^2 increase with N for the GNP systems with random NP starting configurations, indicating that the polymer coronas are becoming less spherical. In contrast, S_v^2 as well as S_c^2 increase much more slowly with N for the fcc starting configurations and have consistently smaller values compared to the random initial configurations. (Note that $S_v^2 = 0$ for a rhombic dodecahedron, which is the Voronoi cell of the fcc lattice.) Nevertheless, the asphericity parameters remain rather low throughout, with the largest values of $S_v^2 \approx 0.15$ and $S_c^2 \approx 0.06$ for the GNPs with the longest grafts ($N = 212$) initialized from random GNP locations. For all GNP systems with varying ρ_g and fixed chain length $N = 85$, the values of S_v^2 and S_c^2 fluctuate around 0.05 and 0.13 (error is <5%), respectively. Thus, the polymer coronas are close to spherical, supporting our initial assumption of the two-layer model.

The observed dependence of our results on the initial configurations is a strong indicator that the GNP systems have not reached global equilibrium in our simulations. There are two qualitatively different time scales that are evidently well separated from each other. The relaxation of the polymer brushes and the corresponding equilibration of the NPs within their nearest-neighbor cages occur at relatively short time scales, whereas the hopping of NPs between cages and the eventual diffusion of GNPs take place on much longer time scales. Indeed, independent experimental rheology measurements of similar GNPs revealed that these cage rearrangements occur on macroscopic time scales (up to several days in some cases).[55] In our simulations, we have achieved the first stage of equilibration, that is, local relaxation of the grafted chains, but the entire system has not reached equilibrium.

To further analyze the distribution of the grafted polymers around the NPs, we computed radial monomer density profiles for the GNP systems with varying grafted chain lengths and grafting densities, as shown in Figure 7a–c. Here, we decompose the monomer density into two parts, $\rho = \rho_s + \rho_o$, where ρ_s is the contribution from polymers grafted to the same NP, while the contribution from other polymers is expressed in ρ_o. In all investigated cases, the total monomer density ρ fluctuates around the average monomer density in the system within our measurement uncertainty. For high grafting density $\rho_g = 0.47\ \sigma^{-2}$, we can see a distinct layering of monomers near the hard NP surface (see Figure 7a,b), which decays within the range of a few monomers. However, no such layering is observed around the NP surface at the lowest grafting density $\rho_g = 0.15\ \sigma^{-2}$ (see Figure 7c). Further, in all cases, ρ_s decays to zero at a distance $r \approx r_{nn} - 2R$, which indicates that the polymers fill the space between neighboring GNPs but do not wrap around them for the chosen set of simulation parameters. For $\rho_g = 0.47\ \sigma^{-2}$, ρ_o approaches zero as we move toward the NP surface, because the cores of the GNPs are completely surrounded by their own monomers. For $\rho_g = 0.15\ \sigma^{-2}$, the surrounding polymers from the other cores can easily interpenetrate, resulting in nonzero values of ρ_o even close to the NP surface (see Figure 7c). For comparison, the radial density profiles for the fcc lattice starting configurations are presented in Figure 7a,b as dashed lines, and we can see only minor deviations between the two cases.

To quantify the interpenetration of polymer coronas from neighboring GNPs, we computed the product of the radial monomer density profiles, $\rho_s\rho_o$, which is shown in Figure 7a–c as orange lines. The full width at half-maximum, δ, of the product of $\rho_s\rho_o$ provides a measure for the width of the interpenetration layer. We use the location of the maximum (corresponding to the distance where ρ_s and ρ_o cross) to extract the overall brush thickness, h_ρ. In Figure 7a,b, we have presented results from random and fcc lattice starting configurations. In both cases, the maxima of the distributions appear at similar locations and thus provide similar values for the total brush thickness h_ρ, indicating that h_ρ does not depend on the starting configurations. Further, we identify the thickness of the dry layer by $h_{dry} = h_\rho - \delta/2$ and attribute the remaining part of the brush thickness to the interpenetration layer, that is, $h_{inter}/2 = h_\rho - h_{dry} = \delta/2$. Following this convention, the typical fraction of monomers from other
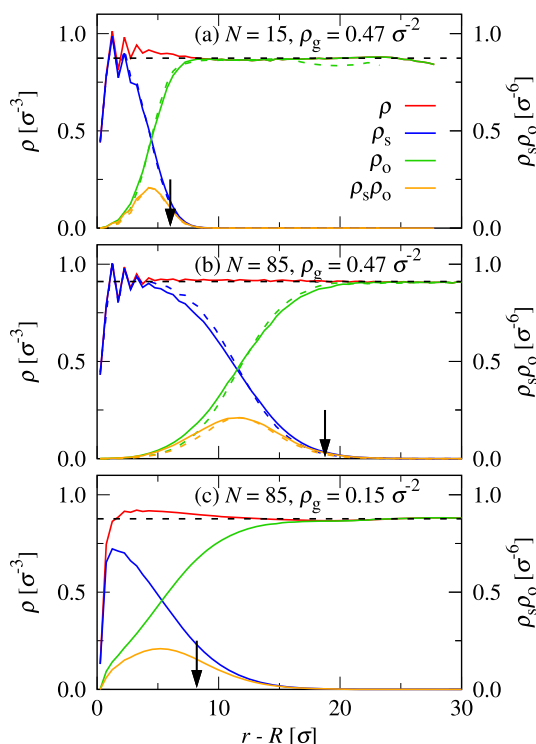
Figure 7. Monomer density profiles of the grafted polymers around the NPs as a function of radial distance from the surface of the NPs, $r - R$, for various grafted chain lengths and grafting densities, (a) $N = 15$, $\rho_g = 0.47\,\sigma^{-2}$; (b) $N = 85$, $\rho_g = 0.47\,\sigma^{-2}$; and (c) $N = 85$, $\rho_g = 0.15\,\sigma^{-2}$. Here, ρ is the local monomer density, ρ_s is the monomer density of the chains coming from the central NP, and ρ_o is the monomer density from other GNPs. Interpenetration layers are quantified by the product of monomer density profiles, $\rho_s\rho_o$, which are represented by orange lines. Solid and dashed colored lines show the results for random and fcc starting configuration, respectively. The horizontal black dashed line represents the average monomer density in the GNP systems. Black vertical arrows represent the average surface-to-surface distance between neighboring NPs, $r_{nn} - 2R$.

GNPs in the dry layer is 5−6% for all investigated cases (note that the two-layer model assumed strictly 0% and a sharp boundary between the dry and interpenetration layers). The resulting layer thicknesses are plotted in Figure 2a,b, which are in excellent agreement with the theoretical predictions. We also compute the average number of monomers (grafted to the same NP) in the dry layer, n_{dry}, and the average number of monomers $n_{inter} = N − n_{dry}$ in the interpenetration layer.

Next, we compare three different measures of the total brush thickness obtained from our simulations: (i) $h_v = [3\langle V_v \rangle / (4\pi)]^{1/3} − R$ is obtained by the Voronoi construction around the center of the NPs, assuming that the Voronoi cells are spherical (same definition as in our two-layer model); (ii) $h_{nn} = r_{nn}/2 − R$ has been extracted from the first peak of the radial distribution function between the NPs (see Figure 5); and (iii) h_ρ is the radially averaged location of the crossing of ρ_s and ρ_o, which corresponds to the center of the interpenetration layer formed by the polymer brushes of adjacent GNPs. The values for h_v, h_{nn}, and h_ρ are listed in Table 1 for all simulated systems, with $h_{nn} < h_\rho < h_v$. We used h_ρ to define the brush thickness in our simulations and all quantities derived from it. The differences between these values can be understood by considering the rhombic dodecahedral shape of the Voronoi

cells in the simulations with fcc starting configurations (see Figure 1b and Supporting Information for details): The thickness h_{nn} corresponds to half of the face-to-face distance of the Voronoi cell, and for a perfect rhombic dodecahedron it is given by $h_{nn} = (\pi/\sqrt{18})^{1/3}R_{tot} − R \approx 0.9R_{tot} − R < R_{tot} − R = h_v$. If the crossing of ρ_s and ρ_o occurs exactly on the surface of the rhombic dodecahedron, then geometric considerations lead to $h_\rho \approx 1.115(\pi/\sqrt{18})^{1/3}R_{tot} − R > h_v$. We found, however, that these crossings occur at slightly shorter distances compared to the surface of a perfect rhombic dodecahedron, so that the measured h_ρ is somewhat smaller than theoretically expected. To account for this discrepancy, we introduce an empirical shape factor $\alpha \approx 0.93$ based on our simulation results, and multiply all theoretical expressions for the brush thickness (i.e., h, h_{dry}, and $h_{inter}/2$) by this factor.

Figure 8a shows the values of the fraction of monomers in the interpenetration zone n_{inter}/N as functions of N at fixed ρ_g
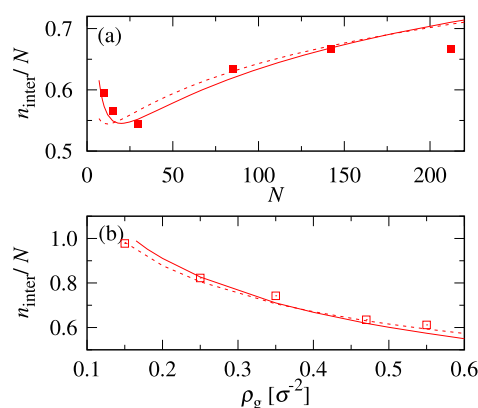

Figure 8. Fraction of monomers in the interpenetration zone n_{inter}/N as a function of (a) N at fixed $\rho_g = 0.47\,\sigma^{-2}$ and (b) ρ_g at fixed $N = 85$. The symbols show the simulation results (initialized from random NP locations), and the solid lines indicate the theoretical prediction from our two-layer model. The dashed lines are the theoretical predictions of the modified model of Kapnistos et al.[25]

$= 0.47\,\sigma^{-2}$. The results from theory and simulation are in good agreement with each other, exhibiting the same trends: For small N, the ratio n_{inter}/N decreases with N due to the faster growth of the dry layer in this regime, while n_{inter}/N gradually increases with N for large N, resulting in a minimum at intermediate N. Note that $\phi_{inter}(N)$ decays monotonically with increasing N for the same parameters (cf. Figure 2d), as the calculation of ϕ_{inter} includes the NP core in the denominator as discussed in the Two-Layer Model section. The values of n_{inter}/N for the GNP systems with varying ρ_g at fixed $N = 85$ are plotted in Figure 8b. In this case, both the theory and the simulations show that n_{inter}/N gradually decreases with increasing grafting density ρ_g for fixed N.

To better understand the conformational details of the grafted chains, we computed the polymer end-to-end vector $\mathbf{R}_e$ and its radial ($R_{e,r}$) and transverse ($R_{e,t}$) components, both for the entire chains and for chain segments of length n. We first determined from our simulation data the probability distribution functions of the squared end-to-end distances of the entire grafted chains, $P(\langle R_e^2 \rangle)$, revealing that the grafted chains are always more extended than polymers of the same length in a pure melt (see Figure S5 in Supporting Information). Chain sections close to the NP surface have

different conformations compared to chain sections at the periphery of the polymer corona because of steric crowding effects. To quantify the local polymer conformation, we have computed $\langle R_{e,r} \rangle$ for subsections of fixed length $n = 20$ along the chain contour. Figure 9 shows $\langle R_{e,r} \rangle^2$ of these chain
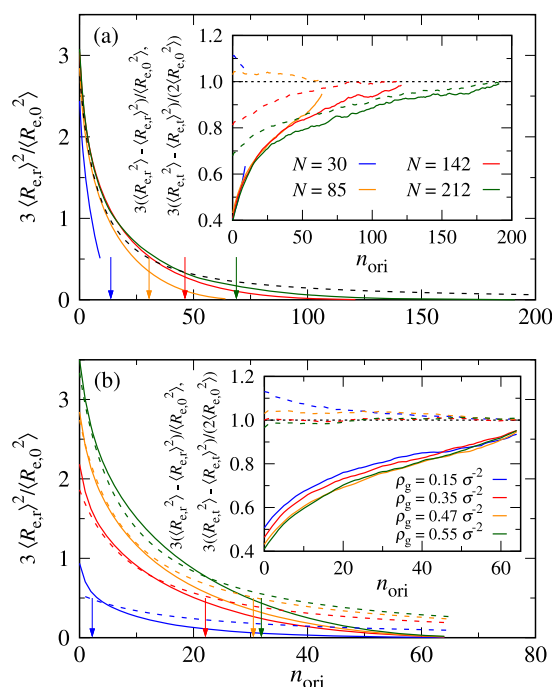

Figure 9. Main plots: Square of normalized average radial end-to-end distances $3\langle R_{e,r}\rangle^2/\langle R_{e,0}^2\rangle$ in chain sections of length n. The dashed lines correspond to the theoretical prediction from our two-layer model $3[h(n_{ori} + n) - h(n_{ori})]^2/(nb^2)$, while vertical colored arrows indicate n_{dry} from our simulations. Insets: Normalized fluctuations of the radial (solid) and transverse (dashed) components of the end-to-end vector, $3(\langle R_{e,r}^2\rangle - \langle R_{e,r}\rangle^2)/\langle R_{e,0}^2\rangle$ and $3(\langle R_{e,t}^2\rangle - \langle R_{e,t}\rangle^2)/(2\langle R_{e,0}^2\rangle)$, respectively. In all panels, the chain section length is fixed at $n = 20$ with one chain end at monomer n_{ori} and the other end at monomer $n_{ori} + n$. Data shown for GNP systems with (a) $N = 30, 85, 142,$ and 212 at $\rho_g = 0.47\ \sigma^{-2}$ and (b) $\rho_g = 0.15\ \sigma^{-2}, 0.35\ \sigma^{-2}, 0.47\ \sigma^{-2},$ and $0.55\ \sigma^{-2}$ at $N = 85$.

sections (the average transverse components $\langle R_{e,t} \rangle$ are always zero within statistical fluctuations), normalized by the mean-square end-to-end distance in a pure polymer melt $\langle R_{e,0}^2(n)\rangle/3$. All results are shown as functions of the chain section origin n_{ori} ($n_{ori} = 0$ corresponds to the grafting point) for GNP systems with (a) varying N at $\rho_g = 0.47\ \sigma^{-2}$ and (b) varying ρ_g at $N = 85$. In our two-layer model, $3\langle R_{e,r}\rangle^2/\langle R_{e,0}^2\rangle = 3[h(n_{ori} + n) - h(n_{ori})]^2/(nb^2)$, which is also included in Figure 9. In Figure S6 of the Supporting Information, we have plotted $3\langle R_{e,r}\rangle^2/\langle R_{e,0}^2\rangle$ as functions of the number n of monomers in a chain section, while fixing one chain end at the grafting point ($n_{ori} = 0$).

In both theory and simulations, there is a pronounced extension of chain sections near the NP surface in all cases, followed by a monotonic decrease of $3\langle R_{e,r}\rangle^2/\langle R_{e,0}^2\rangle$ with increasing n_{ori}. For a given n_{ori}, $3\langle R_{e,r}\rangle^2/\langle R_{e,0}^2\rangle$ increases with increasing grafting density ρ_g in both the dry and interpenetration layer of the polymer corona. In our simulations, chain sections deep in the interpenetration layer approach $\langle R_{e,r}\rangle^2 \approx 0$, whereas $\langle R_{e,r}\rangle^2 > 0$ in our two-layer model for all

n_{ori}. Further, the theoretical extension of chain sections was independent of the total chain length N, which is a consequence of our approximation that all grafted chains behave in the same way and uniformly fill the volume between $h(n_{ori})$ and $h(n_{ori} + n)$. We have also computed the fluctuations of the radial and transverse components of $\mathbf{R}_e(n)$ of these chain sections relative to fluctuations in pure polymer melts, $3(\langle R_{e,r}^2\rangle - \langle R_{e,r}\rangle^2)/\langle R_{e,0}^2\rangle$ and $3(\langle R_{e,t}^2\rangle - \langle R_{e,t}\rangle^2)/(2\langle R_{e,0}^2\rangle)$, respectively. These data are shown in the inset of Figure 9 as functions of n_{ori} for fixed $n = 20$, demonstrating that the fluctuations along the radial direction are strongly suppressed in all cases. In contrast, transverse fluctuations were slightly enhanced for $N \leq 85$ but suppressed for $N > 85$. Figure S6a,b in the Supporting Information shows the square of the normalized average radial size as functions of n at fixed $n_{ori} = 0$, while the relative fluctuations are plotted in Figure S6c,d.

CONCLUSIONS

In this work, we studied the structure of polymer-grafted nanoparticles (GNPs) *via* coarse-grained molecular dynamics simulations by systematically varying the degree of polymerization of the grafted polymers and their grafting density at fixed NP radii. The total brush thickness of the GNPs, h, was decomposed into two separate layers: a *dry layer* of extended chains, where only few monomers from the surrounding GNPs were present, and an *interpenetration layer* of unperturbed chains, where significant overlap between grafted chains of the surrounding GNPs occurred, presumably to maximize their conformational entropy. The thicknesses of the dry layer, h_{dry}, and of the interpenetration layer, h_{inter}, were estimated by a simple spherical two-layer model. According to our theory, the behavior of h, h_{dry}, and h_{inter} can be described by a single universal parameter, x, which compares the actual number of graft chains on an NP, Z, to what is expected for the number of overlapping unperturbed chains in a melt with the same volume as the GNP (with both the core and corona included). This crowding parameter x decreases with increasing graft length N at fixed grafting density ρ_g, whereas x increases with increasing ρ_g at fixed N. Thus, $x \approx 1$ for unperturbed chains (*e.g.*, sparsely grafted NPs with long grafts), while $x \gg 1$ for strongly extended chains (*e.g.*, densely grafted NPs with short grafts). We find that this two-layer model works well in the range of our simulations $1 \lesssim x \lesssim 7$.

For GNPs with fixed grafting density ρ_g, both h_{dry} and $h_{inter}/2$ increase with increasing N, with $h_{dry} > h_{inter}/2$ for the investigated range of N at $\rho_g = 0.47\ \sigma^{-2}$. When the chain length N is fixed and ρ_g is varied instead, h_{dry} increases with increasing ρ_g, whereas $h_{inter}/2$ decreases. For sufficiently small ρ_g, h_{dry} is smaller than $h_{inter}/2$, but these two curves cross at some intermediate ρ_g so that eventually $h_{inter}/2 > h_{dry}$ at a large enough ρ_g. We also predict that the volume fraction of the interpenetration layer, ϕ_{inter}, is a universal function of x which decays monotonically with increasing x. All of these predictions from our two-layer scaling model are in quantitative agreement with simulation results after we account for the slightly distorted shape of the polymer coronas. Most importantly, we predict a peak in the chain extension energy $3k_B T h^2/(2Nb^2)$ at $N_{max} \approx 81(\rho R^3)/Z$, which for our system with $\rho_g = 0.47\ \sigma^{-2}$, $R = 7.5\sigma$, $\rho = 0.9\ \sigma^{-3}$ is $N_{max} \approx 93$. For grafts with $N = N_{max}$, the total brush thickness is $h = \sqrt{3}R$, independent of grafting density ρ_g and monomer density ρ. The associated maximum value of the extension energy is E_{ext}

$\approx 0.055\alpha^2 k_B TZ/(\rho R b^2)$, which is $\approx 1.4\ k_B T$ for our case ($Z = 332$, $\alpha \approx 0.93$).

Our theoretical model is useful for designing pure melts of GNPs with tailored structural properties, for instance, optimizing the degree of polymer interpenetration at a given NP volume fraction. Further, the theoretical knowledge gained from this work provides a starting point for investigating systems to which additional free components, such as small molecules or ungrafted polymers, are added. For example, it is conceivable that small additives become homogeneously dispersed in the polymer brush, whereas large additives could occupy the interstitial sites between the polymer coronas. A conjecture could be that the optimal condition for this partitioning to occur is at the maximum chain extension energy. It will also be interesting to investigate the structural properties of anisotropic GNPs with high aspect ratios.

METHODS

The grafted polymers are represented by a bead–spring model, where a chain consists of N spherical beads, each with diameter σ and mass m. The bonds between the individual monomers are modeled via the finitely extensible nonlinear elastic (FENE) potential:[56,57]

$$U_{FENE}(r) = -\frac{k}{2}r_0^2 \ln\left[1 - \left(\frac{r}{r_0}\right)^2\right] \tag{19}$$

where r_0 is the maximum bond length and k is the spring constant. To prevent unphysical bond crossing, which will impact our associated study on system dynamics, we employed the standard Kremer–Grest parametrization,[56,57] that is, $r_0 = 1.5\sigma$ and $k = 30\varepsilon/\sigma^2$.

The interaction between any two monomers separated by distance r is represented by the standard Lennard-Jones (LJ) potential:

$$U_{MM}(r) = \begin{cases} 4\varepsilon\left[\left(\frac{\sigma}{r}\right)^{12} - \left(\frac{\sigma}{r}\right)^6\right] & \text{for } r \leq r_c \\ 0 & \text{for } r > r_c \end{cases} \tag{20}$$

with cutoff distance $r_c = 3\sigma$, and interaction strength $\varepsilon = k_B T$. The pair potential $U_{MM}(r)$ is multiplied with a smoothing polynomial, $S(r)$, for distances $r \geq r_{sm} = 2.5\sigma$, to gradually decrease both the potential and force to zero at $r = r_c$. The functional form of $S(r)$ is:

$$S(r) = \frac{(r_c^2 - r^2)^2(r_c^2 + 2r^2 - 3r_{sm}^2)}{(r_c^2 - r_{sm}^2)^3} \tag{21}$$

The hard NPs are modeled as smooth spheres with radius R. The NP–NP interaction is described by the shifted Lennard-Jones (sLJ) potential:

$$U_{NN}(r) = \begin{cases} 4\varepsilon\left[\left(\frac{2R}{r-\Delta}\right)^{12} - \left(\frac{2R}{r-\Delta}\right)^6\right] & \text{for } r \leq r_{SLJ} + \Delta \\ 0 & \text{for } r > r_{SLJ} + \Delta \end{cases} \tag{22}$$

with $\Delta = 2R - 1$ and cutoff distance $r_{SLJ} = 2^{1/6}\sigma$ to make U_{NN} purely repulsive. The interaction between a monomer and an NP is also described by the sLJ potential with $\Delta = (2R + \sigma)/2 - 1$ in eq 22.

The polymers are grafted to the NPs by rigidly attaching the first polymer bead to the NP surface. These immobile grafting points are randomly distributed on the NP surface with a minimum distance of σ. Then, the remainder of the chains are connected to those grafting beads using the FENE potential (see the schematic representation given in Figure 10).

Throughout all our simulations, we set the radius of the NPs to $R = 7.5\sigma$ and either varied the degree of polymerization N at fixed grafting
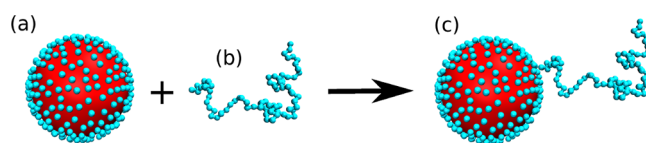

Figure 10. Schematic of (a) an NP with all grafting beads, (b) a polymer chain which will be grafted to the NP surface, and (c) the resulting GNP with one grafted chain.

density $\rho_g = 0.47\ \sigma^{-2}$ or varied ρ_g at fixed $N = 85$ (a summary of the simulated systems is given in Table 2). Note that for $\sigma = 1$ nm, this model matches the experimental systems studied by Bilchak et al.[51] All our MD simulations are performed using the HOOMD-blue software package (v. 2.5.1) with double-precision floating point operations.[58–60] Periodic boundary conditions are applied along the x, y, and z directions. We set the simulation time step to $\Delta t = 0.002\tau$, where $\tau = \sqrt{m\sigma^2/(k_B T)}$ is the intrinsic MD unit of time.

In order to study the effect of the NP arrangement, we generated starting configurations where the GNPs are either placed randomly in the simulation box or on the fcc lattice. Initially, N_{NP} GNPs are distributed in a cubic box, with its edge length chosen such that the polymer coronas of the GNPs do not overlap. Next, an isotropic compression is applied, until we reach a monomer density (typically between 0.7 σ^{-3} and 0.8 σ^{-3}) close to the one at equilibrium, $\rho \approx 0.9$ σ^{-3}. During this process, all interactions are set to purely repulsive. In the next step, we turn on the attractive contributions of the pair potentials, and simulate over 2×10^7 time steps in the NPT ensemble at fixed pressure $P = 0\ \varepsilon/\sigma^3$ and temperature $T = \varepsilon/k_B$. After equilibrating the system in the NPT ensemble, we compute the time-averaged volume of the system, and simulate for 10^7 time steps at this volume in the NVT ensemble, using a Langevin thermostat. For the final production runs, we perform simulations in the NVE ensemble for at least 5×10^7 time steps. The volume fraction of NPs in the system is then $\phi_{NP} = 4\pi R^3 N_{NP}/(3V)$. All results presented for the GNP systems with random starting configurations are averaged over three independent initializations, while we use a single starting configuration for the systems initialized on the fcc lattice. We found that the final box volume, and thus also the monomer density ρ and NP loading ϕ_{NP}, did not depend on the starting configuration.

ASSOCIATED CONTENT

ⓢ Supporting Information

The Supporting Information is available free of charge at https://pubs.acs.org/doi/10.1021/acsnano.0c06134.

Detailed derivation of the two-layer model; discussion of determination of brush thickness in simulations; additional information on end-to-end distances of grafted polymer chains; and comparison of scaling models (PDF)

AUTHOR INFORMATION

Corresponding Authors

Arash Nikoubashman − Institute of Physics, Johannes Gutenberg University Mainz, Mainz 55128, Germany; ⓞ orcid.org/0000-0003-0563-825X; Email: anikouba@uni-mainz.de

Jiarul Midya − Institute of Physics, Johannes Gutenberg University Mainz, Mainz 55128, Germany; ⓞ orcid.org/0000-0003-1695-9059; Email: jimidya@uni-mainz.de

Authors

Michael Rubinstein − Thomas Lord Department of Mechanical Engineering and Materials Science, Biomedical Engineering, Chemistry, and Physics, Duke University, Durham, North Carolina 27708-0300, United States; Institute for Chemical

Reaction Design and Discovery, Hokkaido University, Sapporo 001-0021, Japan

Sanat K. Kumar − *Department of Chemical Engineering, Columbia University, New York, New York 10027, United States;* ⬤ orcid.org/0000-0002-6690-2221

Notes
The authors declare no competing financial interest.

REFERENCES

(1) Allen, T. M.; Cullis, P. R. Drug Delivery Systems: Entering the Mainstream. *Science* **2004**, *303*, 1818−1822.

(2) De, M.; Ghosh, P. S.; Rotello, V. M. Applications of Nanoparticles in Biology. *Adv. Mater.* **2008**, *20*, 4225−4241.

(3) Sun, T.; Zhang, Y. S.; Pang, B.; Hyun, D. C.; Yang, M.; Xia, Y. Engineered Nanoparticles for Drug Delivery in Cancer Therapy. *Angew. Chem., Int. Ed.* **2014**, *53*, 12320−12364.

(4) Galizia, M.; Chi, W. S.; Smith, Z. P.; Merkel, T. C.; Baker, R. W.; Freeman, B. D. 50th Anniversary Perspective: Polymers and Mixed Matrix Membranes for Gas and Vapor Separation: A Review and Prospective Opportunities. *Macromolecules* **2017**, *50*, 7809−7843.

(5) Pandey, N.; Shukla, S. K.; Singh, N. B. Water Purification by Polymer Nanocomposites: An Overview. *Nanocomposites* **2017**, *3*, 47−66.

(6) Barnett, J. W.; Kumar, S. K. Modeling Gas Transport in Polymer-Grafted Nanoparticle Membranes. *Soft Matter* **2019**, *15*, 424−432.

(7) Hosein, I. D.; Lee, S. H.; Liddell, C. M. Dimer-Based Three-Dimensional Photonic Crystals. *Adv. Funct. Mater.* **2010**, *20*, 3085−3091.

(8) Ding, T.; Song, K.; Clays, K.; Tung, C.-H. Fabrication of 3D Photonic Crystals of Ellipsoids: Convective Self-Assembly in Magnetic Field. *Adv. Mater.* **2009**, *21*, 1936−1940.

(9) Beltramo, P. J.; Schneider, D.; Fytas, G.; Furst, E. M. Anisotropic Hypersonic Phonon Propagation in Films of Aligned Ellipsoids. *Phys. Rev. Lett.* **2014**, *113*, 205503.

(10) Kim, H.; Cang, Y.; Kang, E.; Graczykowski, B.; Secchi, M.; Montagna, M.; Priestley, R. D.; Furst, E. M.; Fytas, G. Direct Observation of Polymer Surface Mobility *via* Nanoparticle Vibrations. *Nat. Commun.* **2018**, *9*, 2918.

(11) Green, D. L.; Mewis, J. Connecting the Wetting and Rheological Behaviors of Poly(dimethylsiloxane)-Grafted Silica Spheres in Poly(dimethylsiloxane) Melts. *Langmuir* **2006**, *22*, 9546−9553.

(12) Akcora, P.; Liu, H.; Kumar, S. K.; Moll, J.; Li, Y.; Benicewicz, B. C.; Schadler, L. S.; Acehan, D.; Panagiotopoulos, A. Z.; Pryamitsyn, V.; Ganesan, V.; Ilavsky, J.; Thiyagarajan, P.; Colby, R. H.; Douglas, J. F. Anisotropic Self-Assembly of Spherical Polymer-Grafted Nanoparticles. *Nat. Mater.* **2009**, *8*, 354−359.

(13) Agarwal, P.; Qi, H.; Archer, L. A. The Ages in a Self-Suspended Nanoparticle Liquid. *Nano Lett.* **2010**, *10*, 111−115.

(14) Kim, D.; Archer, L. A. Nanoscale Organic-Inorganic Hybrid Lubricants. *Langmuir* **2011**, *27*, 3083−3094.

(15) Kumar, S. K.; Jouault, N.; Benicewicz, B.; Neely, T. Nanocomposites with Polymer Grafted Nanoparticles. *Macromolecules* **2013**, *46*, 3199−3214.

(16) Chandran, S.; Saw, S.; Kandar, A. K.; Dasgupta, C.; Sprung, M.; Basu, J. K. Suspensions of Polymer-Grafted Nanoparticles with Added Polymers-Structure and Effective Pair-Interactions. *J. Chem. Phys.* **2015**, *143*, No. 084902.

(17) Choudhury, S.; Agrawal, A.; Kim, S. A.; Archer, L. A. Self-Suspended Suspensions of Covalently Grafted Hairy Nanoparticles. *Langmuir* **2015**, *31*, 3222−3231.

(18) Cheng, S.; Carroll, B.; Bocharova, V.; Carrillo, J.-M.; Sumpter, B. G.; Sokolov, A. P. Focus: Structure and Dynamics of the Interfacial Layer in Polymer Nanocomposites with Attractive Interactions. *J. Chem. Phys.* **2017**, *146*, 203201.

(19) Lenart, W. R.; Hore, M. J. StructureProperty Relationships of Polymer-Grafted Nanospheres for Designing Advanced Nanocomposites. *Nano-Struct. Nano-Objects* **2018**, *16*, 428−440.

(20) Daoud, M.; Cotton, J. P. Star Shaped Polymers: A Model for the Conformation and its Concentration Dependence. *J. Phys. (Paris)* **1982**, *43*, 531−538.

(21) Ohno, K.; Morinaga, T.; Takeno, S.; Tsujii, Y.; Fukuda, T. Suspensions of Silica Particles Grafted with Concentrated Polymer Brush: Effects of Graft Chain Length on Brush Layer Thickness and Colloidal Crystallization. *Macromolecules* **2007**, *40*, 9143−3150.

(22) Zhulina, E. B. Phase Diagram for Semi-Rigid Macromolecules Grafted to a Solid Sphere. *Polym. Sci. U.S.S.R.* **1984**, *26*, 885−891.

(23) Birshtein, T. M.; Zhulina, E. B. Conformations of Star-Branched Macromolecules. *Polymer* **1984**, *25*, 1453−1461.

(24) Birshtein, T. M.; Zhulina, E. B.; Borisov, O. V. Temperature-Concentration Diagram for a Solution of Star-Branched Macromolecules. *Polymer* **1986**, *27*, 1078−1086.

(25) Kapnistos, M.; Semenov, A. N.; Vlassopoulos, D.; Roovers, J. Viscoelastic Response of Hyperstar Polymers in the Linear Regime. *J. Chem. Phys.* **1999**, *111*, 1753−1759.

(26) Rafiee, M. A.; Rafiee, J.; Wang, Z.; Song, H.; Yu, Z.-Z.; Koratkar, N. Enhanced Mechanical Properties of Nanocomposites at Low Graphene Content. *ACS Nano* **2009**, *3*, 3884−3890.

(27) Cheng, S.; Bocharova, V.; Belianinov, A.; Xiong, S.; Kisliuk, A.; Somnath, S.; Holt, A. P.; Ovchinnikova, O. S.; Jesse, S.; Martin, H.; Etampawala, T.; Dadmun, M.; Sokolov, A. P. Unraveling the Mechanism of Nanoscale Mechanical Reinforcement in Glassy Polymer Nanocomposites. *Nano Lett.* **2016**, *16*, 3630−3637.

(28) Ethier, J. G.; Hall, L. M. Structure and Entanglement Network of Model Polymer-Grafted Nanoparticle Monolayers. *Macromolecules* **2018**, *51*, 9878−9889.

(29) Ji, T.; Ma, C.; Brisbin, L.; Dong, Y.; Zhu, J. Effect of Interface on the Mechanical Behavior of PolybutadieneSilica Composites: An Experimental and Simulation Study. *J. Appl. Polym. Sci.* **2018**, *135*, 46089.

(30) Midya, J.; Cang, Y.; Egorov, S. A.; Matyjaszewski, K.; Bockstaller, M. R.; Nikoubashman, A.; Fytas, G. Disentangling the Role of Chain Conformation on the Mechanics of Polymer Tethered Particle Materials. *Nano Lett.* **2019**, *19*, 2715−2722.

(31) Hansoge, N. K.; Huang, T.; Sinko, R.; Xia, W.; Chen, W.; Keten, S. Materials by Design for Stiff and Tough Hairy Nanoparticle Assemblies. *ACS Nano* **2018**, *12*, 7946−7958.

(32) Yang, S.; Akcora, P. Deformation of Chemically Heterogeneous Interfacial Layers of Polymer Nanocomposites. *ACS Macro Lett.* **2019**, *8*, 1635−1641.

(33) Bilchak, C. R.; Huang, Y.; Benicewicz, B. C.; Durning, C. J.; Kumar, S. K. High-Frequency Mechanical Behavior of Pure Polymer-Grafted Nanoparticle Constructs. *ACS Macro Lett.* **2019**, *8*, 294−298.

(34) Li, Y.; Tao, P.; Viswanath, A.; Benicewicz, B. C.; Schadler, L. S. Bimodal Surface Ligand Engineering: The Key to Tunable Nanocomposites. *Langmuir* **2013**, *29*, 1211−1220.

(35) Wang, Z.; Lu, Z.; Mahoney, C.; Yan, J.; Ferebee, R.; Luo, D.; Matyjaszewski, K.; Bockstaller, M. R. Transparent and High Refractive Index Thermoplastic Polymer Glasses Using Evaporative Ligand

Exchange of Hybrid Particle Fillers. *ACS Appl. Mater. Interfaces* **2017**, *9*, 7515−7522.

(36) McGrail, B. T.; Sehirlioglu, A.; Pentzer, E. Polymer Composites for Thermoelectric Applications. *Angew. Chem., Int. Ed.* **2015**, *54*, 1710−1723.

(37) Sunday, D. F.; Green, D. L. Thermal and Rheological Behavior of Polymer Grafted Nanoparticles. *Macromolecules* **2015**, *48*, 8651−8659.

(38) Grabowski, C. A.; Koerner, H.; Meth, J. S.; Dang, A.; Hui, C. M.; Matyjaszewski, K.; Bockstaller, M. R.; Durstock, M. F.; Vaia, R. A. Performance of Dielectric Nanocomposites: Matrix-Free, Hairy Nanoparticle Assemblies and Amorphous PolymerNanoparticle Blends. *ACS Appl. Mater. Interfaces* **2014**, *6*, 21500−21509.

(39) Kim, S. A.; Mangal, R.; Archer, L. A. Relaxation Dynamics of Nanoparticle-Tethered Polymer Chains. *Macromolecules* **2015**, *48*, 6280−6293.

(40) Wood, A. B. *A Textbook of Sound; Being an Account of the Physics of Vibrations with Special Reference to Recent Theoretical and Technical Developments*, 2nd ed.; The Macmillan Company: New York, 1941.

(41) Kumar, S. K.; Krishnamoorti, R. Nanocomposites: Structure, Phase Behavior, and Properties. *Annu. Rev. Chem. Biomol. Eng.* **2010**, *1*, 37−58.

(42) Chremos, A.; Panagiotopoulos, A. Z. Structural Transitions of Solvent-Free Oligomer-Grafted Nanoparticles. *Phys. Rev. Lett.* **2011**, *107*, 105503.

(43) Ganesan, V.; Jayaraman, A. Theory and Simulation Studies of Effective Interactions, Phase Behavior and Morphology in Polymer Nanocomposites. *Soft Matter* **2014**, *10*, 13−38.

(44) Chremos, A.; Douglas, J. F. Self-Assembly of Polymer-Grafted Nanoparticles in Solvent-Free Conditions. *Soft Matter* **2016**, *12*, 9527−9537.

(45) Yatsyshin, P.; Fytas, N. G.; Theodorakis, P. E. Mixing-Demixing Transition in Polymer-Grafted Spherical Nanoparticles. *Soft Matter* **2020**, *16*, 703−708.

(46) Koski, J. P.; Krook, N. M.; Ford, J.; Yahata, Y.; Ohno, K.; Murray, C. B.; Frischknecht, A. L.; Composto, R. J.; Riggleman, R. A. Phase Behavior of Grafted Polymer Nanocomposites from Field-Based Simulations. *Macromolecules* **2019**, *52*, 5110−5121.

(47) Hou, G.; Xia, X.; Liu, J.; Wang, W.; Dong, M.; Zhang, L. Designing Superlattice Structure *via* Self-Assembly of One-Component Polymer-Grafted Nanoparticles. *J. Phys. Chem. B* **2019**, *123*, 2157−2168.

(48) Lafitte, T.; Kumar, S. K.; Panagiotopoulos, A. Z. Self-Assembly of Polymer-Grafted Nanoparticles in Thin Films. *Soft Matter* **2014**, *10*, 786−794.

(49) Ma, S.; Hu, Y.; Wang, R. Amphiphilic Block Copolymer Aided Design of Hybrid Assemblies of Nanoparticles: Nanowire, Nanoring, and Nanocluster. *Macromolecules* **2016**, *49*, 3535−3541.

(50) Beltran-Villegas, D. J.; Jayaraman, A. Assembly of Amphiphilic Block Copolymers and Nanoparticles in Solution: Coarse-Grained Molecular Simulation Study. *J. Chem. Eng. Data* **2018**, *63*, 2351−2367.

(51) Bilchak, C. R.; Buenning, E.; Asai, M.; Zhang, K.; Durning, C. J.; Kumar, S. K.; Huang, Y.; Benicewicz, B. C.; Gidley, D. W.; Cheng, S.; Sokolov, A. P.; Minelli, M.; Doghieri, F. Polymer-Grafted Nanoparticle Membranes with Controllable Free Volume. *Macromolecules* **2017**, *50*, 7111−7120.

(52) Chremos, A.; Nikoubashman, A.; Panagiotopoulos, A. Z. Flory-Huggins Parameter χ, From Binary Mixtures of Lennard-Jones Particles to Block Copolymer Melts. *J. Chem. Phys.* **2014**, *140*, No. 054909.

(53) Humphrey, W.; Dalke, A.; Schulten, K. VMD - Visual Molecular Dynamics. *J. Mol. Graphics* **1996**, *14*, 33−38.

(54) Ramasubramani, V.; Dice, B. D.; Harper, E. S.; Spellings, M. P.; Anderson, J. A.; Glotzer, S. C. freud: A Software Suite for High Throughput Analysis of Particle Simulation Data. *Comput. Phys. Commun.* **2020**, *254*, 107275.

(55) Parisi, D.; Buening, E.; Gury, L.; Benicewicz, B. C.; Cloitre, M.; Rubinstein, M.; Kumar, S. K.; Vlassopoulos, D. Jammed Colloidal Dynamics in Self-Suspended Grafted Nanoparticle Melts (unpublished).

(56) Kremer, K.; Grest, G. S. Dynamics of Entangled Linear Polymer Melts: A Molecular-Dynamics Simulation. *J. Chem. Phys.* **1990**, *92*, 5057−5086.

(57) Grest, G. S.; Kremer, K. Molecular Dynamics Simulation for Polymers in the Presence of a Heat Bath. *Phys. Rev. A: At., Mol., Opt. Phys.* **1986**, *33*, 3628−3631.

(58) Anderson, J. A.; Lorenz, C. D.; Travesset, A. General Purpose Molecular Dynamics Simulations Fully Implemented on Graphics Processing Units. *J. Comput. Phys.* **2008**, *227*, 5342−5359.

(59) Glaser, J.; Nguyen, T. D.; Anderson, J. A.; Lui, P.; Spiga, F.; Millan, J. A.; Morse, D. C.; Glotzer, S. C. Strong Scaling of General-Purpose Molecular Dynamics Simulations on GPUs. *Comput. Phys. Commun.* **2015**, *192*, 97−107.

(60) Howard, M. P.; Anderson, J. A.; Nikoubashman, A.; Glotzer, S. C.; Panagiotopoulos, A. Z. Efficient Neighbor List Calculation for Molecular Simulation of Colloidal Systems Using Graphics Processing Units. *Comput. Phys. Commun.* **2016**, *203*, 45−52.